CrossMark

ORIGINAL ARTICLE

Modeling Blood Flow Through Intracranial Aneurysms: A Comparison of Newtonian and Non-Newtonian Viscosity

Gregory Carty[1] · Surapong Chatpun[2] · Daniel M. Espino[1]

Abstract The effect of non-Newtonian blood flow on the value of wall shear stress (WSS) of an intracranial aneurysm was investigated using computational fluid dynamics. For cerebral arteries, blood is often assumed to behave as a Newtonian fluid, though the effects of non-Newtonian flow on the prediction of areas of low WSS associated with aneurysm rupture are not clear. Geometry was based on published data and a Newtonian model validated against experimental results. Newtonian, unrestricted non-Newtonian, and viscosity-limited non-Newtonian models were compared under pulsatile conditions. Peak WSS of the Newtonian model was 28.7 Pa, and the lowest value of peak WSS for the unrestricted non-Newtonian models was 16.5 Pa. Viscosity-limited non-Newtonian models predicted flow velocity and WSS similar to those predicted by the Newtonian model in high-shear-rate regions, though maximum areas of critically low WSS were up to 42 % smaller than those predicted by the Newtonian model. In conclusion, viscosity limits are required to prevent excessive thinning of non-Newtonian models and the effects of non-Newtonian viscosity are significant for blood flow within low-shear-rate regions of an intracranial aneurysm.

Keywords Computational fluid dynamics · Intracranial aneurysm · Non-Newtonian blood · Rheology · Wall shear stress

✉ Daniel M. Espino
  d.m.espino@bham.ac.uk

[1] School of Mechanical Engineering, University of Birmingham, Birmingham B15 2TT, UK

[2] Institute of Biomedical Engineering, Prince of Songkla University, Hat Yai 90110, Thailand

1 Introduction

Intracranial aneurysms affect 5–6 % of the population [1–3], and once ruptured mortality rates are high [2, 4]. Aneurysms are enlargements of the arterial walls [3] that form particularly at bends or bifurcations of blood vessels [5]. It is often assumed that for large blood vessels, the non-Newtonian effects of blood flow are negligible [6–11], and it has been stated that non-Newtonian viscosity can be ignored for vessels wider than 0.5 mm [12]. A number of factors, including hematocrit, plasma viscosity, vascular diameter, and temperature, have been determined to affect blood viscosity [13–15]. However, perhaps the largest contributor to non-Newtonian behaviour is the aggregation of red blood cells that form rouleaux when blood is at rest or subject to low amounts of shearing [16, 17]. These rouleaux are groups of red blood cells that are often said to resemble stacks of coins [16, 18]. The forces binding the rouleaux together are weak and under the application of a shearing force will break up into smaller stacks or individual cells [16, 19]. The level of this dissipation is dependent on the rate of shear [16], and when increased results in lower viscosity [19, 20], a condition known as shear thinning. The non-Newtonian effects of blood flow occur only at low shear (<100 s^{-1}) [19, 21] and once sufficient shearing has been established, blood viscosity approaches a lower limit, commonly taken as the Newtonian viscosity [16, 19].

Aneurysm growth is associated with high wall shear stress (WSS) [5, 22], while plaque deposition in areas of low WSS leads to the degeneration of endothelial cells and is responsible for aneurysm rupture [1, 5, 23]. Valencia et al. [5] reported that a minimum WSS of 2 Pa is required to maintain the aneurismal wall and Shojima et al. [1] stated that degeneration will occur in regions below 1.5 Pa.

Furthermore, Cavazzuti et al. [10] reported that a critical value of 0.5 Pa exists, below which thrombus formation may influence aneurysm rupture.

In vivo measurements of WSS and blood flow within intracranial aneurysms are difficult [7], while magnetic resonance imaging (MRI) flow measurements are not sufficiently accurate [2]. Therefore, computational fluid dynamics (CFD) has been extensively used in the study of intracranial aneurysms [2, 5, 10, 24]. Patient-specific CFD studies are increasingly being used to identify patients at risk of rupture [25]. Van Ooij et al. [2] investigated the flow patterns of a Newtonian fluid through a physical model of an intracranial aneurysm. They compared observations from particle image velocimetry and MRI to those predicted by CFD, concluding that CFD is an acceptable predictor of complex flow patterns. Cavazzuti et al. [10] investigated non-Newtonian flow within a side-wall intracranial aneurysm with reference to stent design, and concluded that non-Newtonian properties are important to avoid underestimating WSS. This directly contradicts the textbook advice to assume Newtonian viscosity [9, 11, 12]. Thus, currently it is not clear whether this finding is applicable to other geometries of intracranial aneurysms. Aneurysms formed at bifurcations, such as the anterior communicating artery (ACA), are of particular interest, as CFD has already been established as a suitable method to study them. However, regions predicted to be at high risk of degeneration, i.e. WSS <2 Pa [1, 10], might change depending on the method used to model the non-Newtonian properties of blood. Furthermore, potential benefits and limitations of different non-Newtonian schemes for modeling the ACA are unknown, including whether these should include viscosity limits [16, 19].

The aim of this study is to determine whether CFD predictions of low-WSS regions for a saccular intracranial aneurysm at a bifurcation of an ACA are sensitive to the viscosity scheme used. Therefore, Newtonian, non-Newtonian, and viscosity-limited non-Newtonian definitions for blood are compared. This study focuses on regions of low WSS, especially on regions with predicted WSS of below the 2 Pa required to maintain wall integrity [1], and below the 0.5 Pa at high risk of degeneration [10]. Furthermore, if models were sensitive to non-Newtonian definitions of blood, this study aimed to determine the feasibility of performing CFD analysis that included subject-specific non-Newtonian blood viscosity. Implementing non-Newtonian viscosity schemes from an individual into a CFD model offers the advantage of making predictions that are specific to the individual based on their specific blood rheology, which opens up potential for clinical translation.

2 Methods

2.1 Geometry

The geometry (Fig. 1) is based on published data [2] and represents a typical saccular aneurysm located at a bifurcation of the ACA in the brain. The inflow and outflow vessels are 2.1 mm in diameter and the maximum exterior dimensions of the sac are 9 mm (length) × 8 mm (diameter). Geometry was created in SolidWorks 2013 (Dassault Systèmes, Waltham, MA, USA).

2.2 Blood Properties: Experimental Measurements

Viscosity was obtained from raw data available for animal (hamster) blood from a previous experimental study by Chatpun and Cabrales [26]. The raw data included blood viscosity and hematocrit level. Chatpun and Cabrales [26] measured the blood viscosity using a cone and plate viscometer (model DV-II+ , Brookfield Engineering Laboratories; Middleboro, MA, USA). During their measurements, temperature was controlled at 37 °C and shear rate was varied from 45 to 750 s^{-1}. They measured the hematocrit level from centrifuged arterial blood samples taken in heparinized capillary tubes (Readacrit Centrifuge, Clay Adams, NJ, USA).

2.3 Blood Properties: Modeling

Blood flow was considered incompressible with a density of 1.00×10^3 kg m^{-3} [2, 7]. Viscosity is known to be temperature-dependent [13] and so it is assumed that the
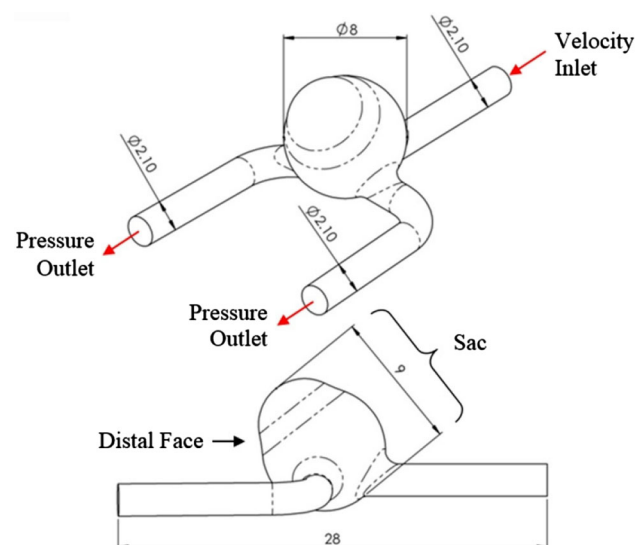
Fig. 1 Aneurysm geometry and dimensions (mm). Also included are boundary conditions; Ø denotes diameter

viscosity values and indices presented reflect blood viscosity at human body temperature. The fluid model was assumed laminar, in line with previous work [5, 10]. Comparisons were made between Newtonian models and a range of non-Newtonian models. For the Newtonian model, blood viscosity was taken from Van Ooij et al. [2] (3.45×10^{-3} Pa s), equivalent to blood of approximately 45 % hematocrit [20]. The non-Newtonian models included unlimited and limited viscosity under power law and Carreau schemes. The viscosity of all non-Newtonian models is shear-rate-dependent. Therefore, the parameters used to define the shear rate dependency of viscosity in Eqs. (1) and (2) are provide in Tables 1, 2 and 3. Further details of all the non-Newtonian models used are given below.

Non-Newtonian flow was modeled using two power law schemes (*PL-Wang* and *PL-Rhe-I*) and a Carreau scheme (*Carreau-I*). These models have been commonly used for modeling blood viscosity [27–30]. These models were used to investigate the power law with no lower limit of viscosity and the effect of consistency index, using parameters from the literature and experimental data. Subsequently, a common viscosity limit was imposed on the non-Newtonian models to investigate the difference between schemes at low shear rates, leading to models *PL-Shibeshi*, *PL-Rhe-II*, and *Carreau-II*. *PL-Shibeshi* replaced *PL-Wang* with new consistency index parameters obtained from the literature.

The power law is a generalised viscosity scheme that depends only on the value of the shear rate at an instant during flow [27]. It is described as:

$$\mu = k\dot{\gamma}^{(n-1)} \tag{1}$$

where μ is the dynamic viscosity (Pa s) and $\dot{\gamma}$ is the shear rate (s^{-1}). The consistency index k (kg s^{n-2} m^{-1}) is analogous to the amplitude of viscosity, where higher values of k indicate more viscous fluids [28]. The index parameter n is dimensionless and describes the non-Newtonian fluid behaviour. When $n < 1$, the fluid is shear-thinning [28].

Two non-limited power law models were used for the preliminary investigation, the first based on values from published research [28] (*PL-Wang*) and the other from rheological blood data (*PL-Rhe-I*) (see Sect. 2.2). A power law trendline was fitted to the rheological data, giving a

Table 1 Non-limited power law parameter values

	PL-Wang [28]	*PL-Rhe-I*
Consistency index k (kg s^{n-2} m^{-1})	0.067	0.022
Power law index n	0.708	0.700

Table 2 Viscosity-limited power law parameter values

	PL-Shibeshi [29]	*PL-Rhe-II*
Consistency index k (kg s^{n-2} m^{-1})	0.017	0.022
Power law index n	0.708	0.700
Viscosity limit μ_∞ ($\times 10^{-3}$ Pa s)	3.45	3.45

Table 3 Carreau model parameter values

	Carreau-I [30]	*Carreau-II*
Time constant λ (s)	3.313	3.313
Power law index n	0.3568	0.3568
Zero shear viscosity μ_0 ($\times 10^{-3}$ Pa s)	56.0	56.0
Viscosity limit μ_∞ ($\times 10^{-3}$ Pa s)	3.50	3.45

coefficient of shear rate equal to k and power index equivalent to $n - 1$ (Table 1).

For the viscosity-limited investigation, a lower viscosity (infinite shear) limit was imposed on the power law schemes equal to the Newtonian value. New parameters were taken from Shibeshi et al. [29] (*PL-Shibeshi*) to replace *PL-Wang* (Table 2).

The Carreau model is another generalised viscosity scheme used to simulate shear-thinning fluid behaviour [27]. It provides a smooth transition between the upper and lower limits of viscosity, defined by a power index. It is given as:

$$\mu = \mu_\infty + (\mu_0 - \mu_\infty)\left[1 + (\lambda\dot{\gamma})^2\right]^{\frac{n-1}{2}} \tag{2}$$

where the constants μ_∞, μ_0, λ, and n determine the non-Newtonian behaviour [30]. The upper and lower limits of viscosity are defined by μ_∞ and μ_0 (Pa s), respectively. The non-Newtonian behaviour is described by the time constant λ (s) and the dimensionless power index n, where $n < 1$. The time constant determines the shear rate at which the viscosity begins to transition into the power index region; typically, lower values of λ result in transition beginning at a higher shear rate [30]. The power index describes the sharpness of the transition between the upper and lower shear limits, where low values of n result in a sharper transition [30].

For the non-limited investigation, *Carreau-I* viscosity parameters were taken from Siebert et al. [30] and were modified in the viscosity-limited investigation (*Carreau-II*) to bring the infinite shear limit μ_∞ in line with the Newtonian value (Table 3).
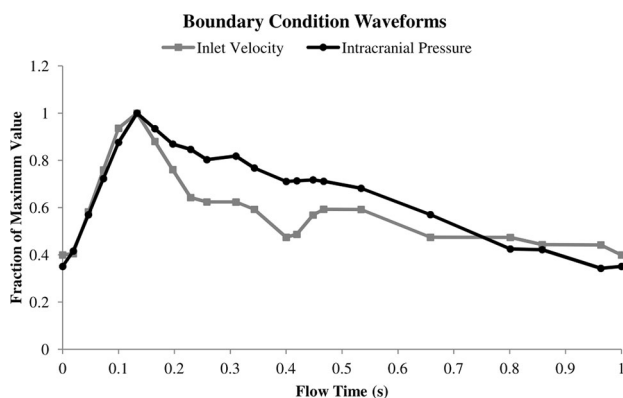
2.4 Boundary Conditions

A steady-state analysis was used to validate the model against experimental data and simulated pre-systolic conditions for the ACA. Inflow velocity was 0.3 m s^{-1} [2] and outlet pressure was 800 Pa (Fig. 1) [31].

Transient analysis was performed by applying time-dependent waveforms, based on data in the literature. Both the inlet velocity [32] and outlet pressure [31] varied with time throughout the cardiac cycle for the ACA, as shown in Fig. 2. A user-defined function was used to apply the boundary conditions for the transient simulations in FLUENT (version 14.5, ANSYS Inc., Canonsburg, PA, USA). The function discretizes the cycle into a series of linear segments and uses adaptive time stepping to run the simulation at predetermined time points. The maximum inflow velocity and outlet pressure occur at a flow time of 0.133 s and have values of 0.679 m s^{-1} and 1.22 kPa, respectively (Figs. 1, 2). Blood vessel walls and the aneurysm sac were modeled as rigid using a no-slip boundary condition [2].

2.5 Mesh and Solution of Governing Equations

The geometry was meshed using the ANSYS Workbench meshing module (ANSYS Inc.). The interior immediately adjacent to the sac walls was meshed with eight-node brick elements using five-layer inflation, and the remainder was meshed using four-node tetrahedral elements. The converged mesh had 214,690 elements. Convergence was assessed as the mesh density that led to flow velocity and mean sac WSS converging to within 1 % of their final values. For example, for the Newtonian model, the mean flow velocity and mean sac WSS converged to within 1 % at 0.121 m s^{-1} and 1.70 Pa, respectively.

Fig. 2 Boundary condition waveforms for inflow velocity and outlet pressure. *Plots* show sampling times used to discretize the cycle. Maximum velocity and pressure are 0.679 m s^{-1} and 1.22 kPa, respectively

The fluid model was laminar and used second-order momentum and pressure formulas using FLUENT, which solves the incompressible Navier–Stokes equations. The assumption of a supine position (i.e., the body is lying horizontally) was used, so that the body force term was omitted from the Navier–Stokes equations. This is a common assumption in blood flow modeling [9, 33]. Fluid was modeled as laminar, though there is evidence to suggest that turbulence within intracranial aneurysms can occur at Reynolds numbers (*Re*) of as low as 400 [34]. This compares to values of around 2300 for flow of a fluid of density ρ at a velocity v through an ordinary pipe of characteristic dimension l (Eq. 3) [24]. Turbulence within cerebral aneurysms contributes to higher WSS [24]. However, peak Reynolds numbers for simulations were lower than the turbulent value, typically ranging from around 150–390 (Table 4), and so the laminar assumption was deemed acceptable.

$$Re = \frac{\rho v l}{\mu} \tag{3}$$

2.6 Validation of Newtonian Model

Predictions from the Newtonian model were compared to experimentally measured values in the literature. The predictions from the Newtonian model of peak velocity and Reynolds number were compared against experimental MRI results [2]. As the geometry used in the present study was based on the dimensions provided in the same study [2], direct comparisons of the results were appropriate.

3 Results

3.1 Newtonian Validation

The Newtonian CFD results were compared against experimental MRI results from the literature [2] (Table 4). The mean velocity of the steady-state CFD model was 0.121 m s^{-1}, approximately 15 % larger than the experimental MRI value (0.105 m s^{-1}). The Reynolds number predicted by the Newtonian model was 325, approximately 25 % higher than the experimental MRI value (261).

The results from the Newtonian model are compared to results from the unlimited non-Newtonian models in Sect. 3.2. Section 3.3 compares the Newtonian model results to predictions from the viscosity-limited models. Finally, the Newtonian model viscosity is compared to the range of non-Newtonian viscosities (which are shear-rate-dependent) in Sect. 3.4.

Table 4 Validation results

Model	Steady-state		Transient			
	Mean velocity (m s^{-1})	Inflow reynolds no.	Mean velocity (m s^{-1})		Inflow reynolds no.	
			Min	Max	Min	Max
Newtonian CFD	0.121	325	0.046	0.216	156	392
Reference MRI [2]	0.105	261	0.030*	0.120*	100*	410*

Values marked with asterisks (*) are quantities estimated from figures in literature

3.2 Unlimited Non-Newtonian

For all models, maximum WSS occurred at peak systole (Figs. 3a, 4a). In general, WSS of *PL-Rhe-I* was the lowest (Fig. 3a) and had a peak value of 16.5 Pa (Fig. 4a). Viscosity of *PL-Rhe-I* at peak WSS was 38 % of the Newtonian value (1.30×10^{-3} Pa s).

PL-Wang predicted the highest WSS (Fig. 3a), with a maximum value of 31.9 Pa (Fig. 4). Furthermore, the mean velocity of *PL-Wang* was substantially lower than those of the other models (Fig. 4b). The highest mean velocity occurred at peak systole and was 0.180 m s^{-1} for *PL-Wang*, compared to 0.220 m s^{-1} for the Newtonian model. The equivalent viscosity at the corresponding shear rate was 53 % larger than the Newtonian value (5.27×10^{-3} Pa s; Fig. 4c).

Under steady-state conditions, the *PL-Wang* model predicted both the smallest area of low WSS (154 mm^2) and the largest area of critically low WSS (19.1 mm^2; Table 5). The distribution of these regions for *PL-Wang* is distinctly different from those for the other models (Fig. 3b).

3.3 Viscosity-Limited Non-Newtonian Models

Mean and maximum flow velocities were similar for all models (Table 6). The Newtonian model predicted the largest values of both (0.121 and 0.535 m s^{-1}, respectively). However, the difference compared to the other schemes was less than 5 %. Likewise, the values of mean and maximum sac WSS were similar (Table 6), and again the Newtonian model predicted the largest values (1.70 and 8.03 Pa, respectively).

All models predicted similar flow patterns. Vortices filled the upper part of the sac and redirected fluid through the bifurcated lumens (Fig. 5a). The resulting WSS distributions were also similar, with the maximum WSS occurring at approximately the same location in each model (Fig. 5b).

The largest area of low WSS was predicted jointly by the Newtonian and *PL- Shibeshi* models (291 mm^2;

Figs. 6, 7a), while the largest area of critically low WSS was predicted by the Newtonian model alone (17.6 mm^2; Figs. 6, 7b). The critically low WSS results exhibited the largest gap between the Newtonian and non-Newtonian models, where at a flow time of 0.97 s (Fig. 6a), the *PL-Rhe-II* prediction was 42 % lower than that of the Newtonian model (Fig. 7b). The smallest areas of low and critically low WSS occurred at peak systole (Fig. 6b).

3.4 Shear Rate Relationships

At high shear rates (>500 s^{-1}), the viscosities of the non-Newtonian schemes are either equal (*PL-Shibeshi*, *PL-Rhe-II*) or very similar (*Carreau-II*) to the Newtonian value (Fig. 8a). The critical shear stress of *PL-Shibeshi* is 0.83 Pa, and that of *PL-Rhe-II* is 1.66 Pa (Fig. 8b). At the low WSS threshold (2 Pa), the *Carreau-II* shear rate is the lowest (510 s^{-1}), while the other schemes have a common shear rate of 580 s^{-1} (Fig. 8b). The lowest shear rate required to produce a stress of 0.5 Pa is found in the *PL-Rhe-II* model (90 s^{-1}; Fig. 8b), which also predicted the smallest area of critically low WSS (Fig. 7b). Likewise, the highest shear rate at 0.5 Pa is found in the Newtonian model (Fig. 7b), which predicted the largest area of critically low WSS (Fig. 7b).

4 Discussion

4.1 Study Findings

This study used CFD to model an intracranial bifurcation with an aneurysm based on published geometry [2]. Uncapped non-Newtonian descriptions were not appropriate for the range of near-wall shear rates within the flow because they underestimate WSS in high-shear-rate regions. Physiologically accurate parameters of non-Newtonian schemes are required to avoid overestimating viscosity. Thus, viscosity-limited parameters were more appropriate because they prevent excessive thinning at high
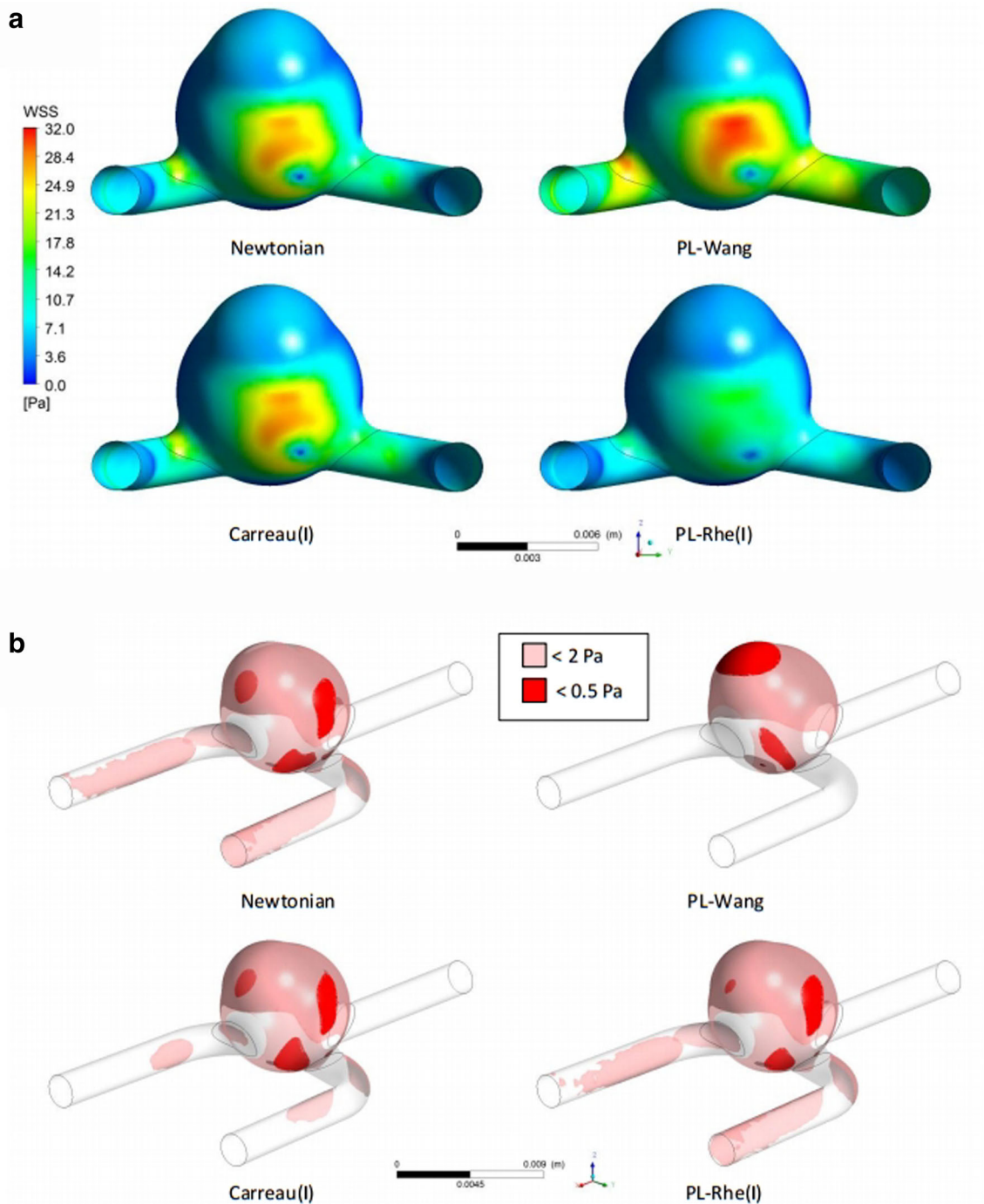
Fig. 3 WSS distribution for unlimited viscosity models. **a** WSS distribution on distal face of aneurysm sac at peak systole. **b** *Plots* of low (<2 Pa) and critically low (<0.5 Pa) WSS under steady-state conditions

shear rates and retain non-Newtonian behaviour at low shear rates. Viscosity-limited non-Newtonian models led to predictions of total area of critically low WSS that were up to 42 % smaller than those predicted by a Newtonian model. This suggests that for more specific predictions to aid surgical practice, non-Newtonian viscosity-limited models may be most appropriate. Moreover, in our study, it was feasible to use subject-specific blood viscosity measurements with the model in order to predict regions of critically low WSS at risk of aneurysm rupture. Therefore, the recommendation is that numerical and computational analysis of treatment strategies for an individual, should characterize a limited non-Newtonian viscosity model for that subject.

Fig. 4 Unlimited viscosity models. **a** Maximum WSS within sac, **b** mean velocity, and **c** viscosity-shear rate relationship
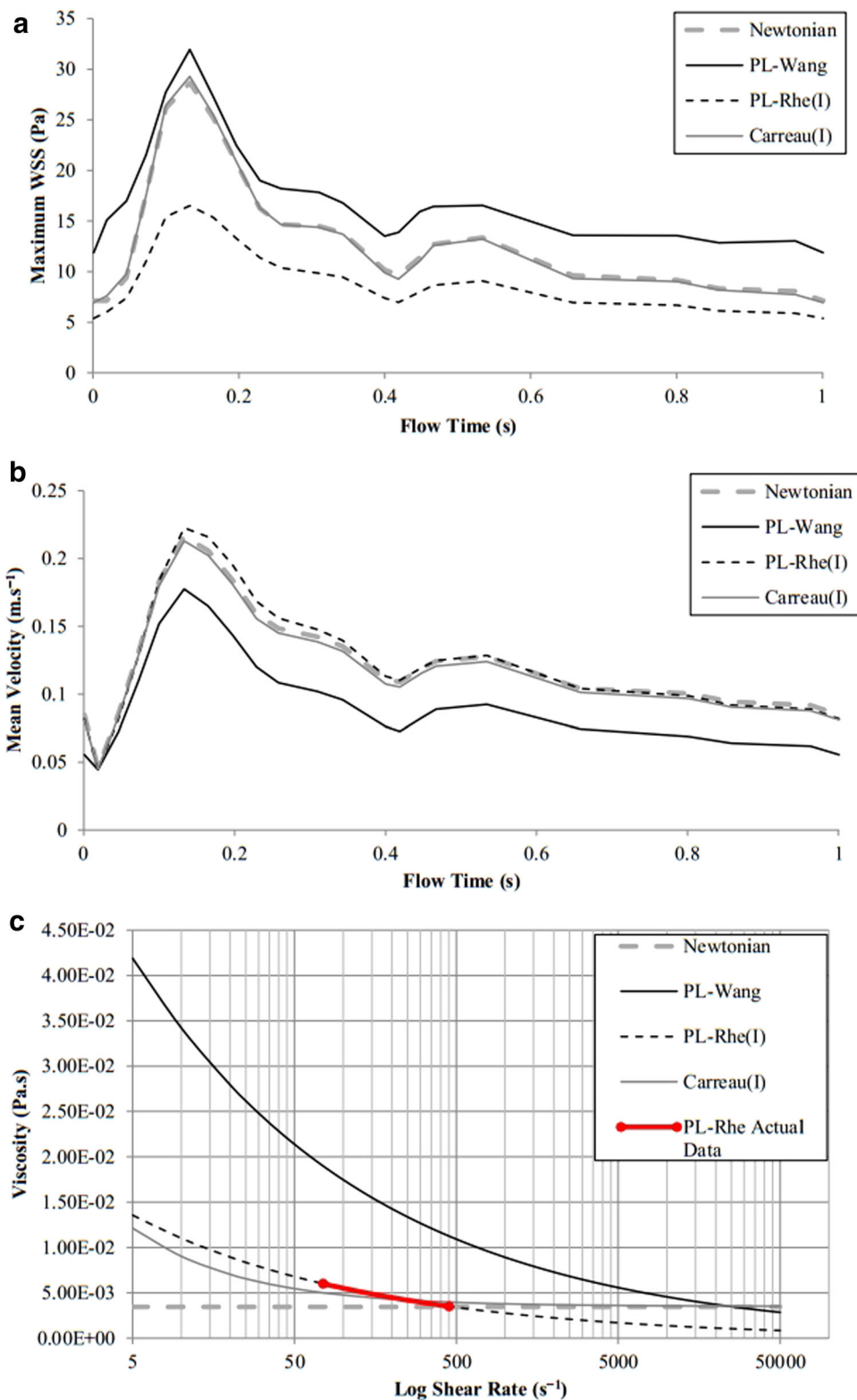
4.2 Blood Viscosity Modeling

Physiologically reliable non-Newtonian parameter values are required to avoid overestimating WSS. The *PL-Wang* consistency index was approximately three times larger than *PL-Rhe-I*. This resulted in substantially higher maximum WSS and lower mean velocity than those obtained by the other models. It also led to altered distribution of the

Table 5 Unlimited models: steady-state results

Viscosity model	Mean sac WSS (Pa)	Max sac WSS (Pa)	Mean velocity (m s^{-1})	Max velocity (m s^{-1})	Low WSS (mm^2)	Crit. low WSS (mm^2)
Newtonian	1.70	8.03	0.121	0.535	232	15.1
PL-Wang	1.79	13.0	0.866	0.529	154	19.1
PL-Rhe-I	1.56	5.97	0.116	0.487	233	10.0
Carreau-I	1.67	7.95	0.115	0.532	182	14.2

Table 6 Viscosity-limited models: steady-state results

Viscosity model	Mean sac WSS (Pa)	Max sac WSS (Pa)	Mean velocity (m s^{-1})	Max velocity (m s^{-1})	Low WSS (mm^2)	Crit. low WSS (mm^2)
Newtonian	1.70	8.03	0.121	0.535	232	15.1
PL-Shibeshi	1.67	7.98	0.119	0.530	232	12.2
PL-Rhe-II	1.67	7.72	0.116	0.522	213	9.91
Carreau-II	1.67	7.92	0.115	0.532	184	13.7

low and critically low WSS regions. There appears to be some consensus that the power law consistency index for blood should be in the region of 0.017 kg s^{n-2} m^{-1} [10, 28, 35]. However, this is not universal, with Johnston et al. [21] using a larger consistency index offset with a lower power index ($k = 0.035$ kg s^{n-2} m^{-1}, $n = 0.6$). The differences that exist between these previous studies are likely the result of different strategies used to characterise blood rheology and the natural variability that exists between different samples. Therefore, the values of parameters that define non-Newtonian blood viscosity should be verified against experimentally obtained rheological data to ensure an accurate representation of blood viscosity. In the present study, non-Newtonian models were successfully implemented using such an approach.

At peak shear rate, the *PL-Rhe-I* model reached a viscosity lower than the Newtonian value and consequently predicted lower maximum WSS than those predicted by the other schemes. This may be a limitation of the power law model [36], as the Carreau models include a limiting parameter that prevented viscosity dropping below the Newtonian value. Likewise, excessive thinning can be avoided by using a viscosity limit on power law models [37]. Gray et al. [37] stated that blood does not get thinner than approximately 3.5×10^{-3} Pa s. The thinnest real blood viscosity identified was 2.85×10^{-3} Pa s [14]. Despite this, some authors have used viscosity limits lower than these values. A Carreau scheme limit of 2.2×10^{-3} Pa s has been used to model the carotid artery [8] and a power law scheme limit of 10^{-5} Pa s has been used for a side-wall intracranial aneurysm [10]. Again, differences are likely the result of different strategies used to

characterize blood rheology and natural variability, further emphasizing the need for characterization of blood rheology, as performed in the present study. If the viscosity limit is underestimated, it will, consequently, underestimate WSS in high-near-wall-shear-rate regions. Therefore, the models used demonstrate the need to apply physiologically appropriate limits to non-Newtonian viscosity.

Viscosity-limited non-Newtonian schemes did not cause large changes in bulk flow velocity or flow patterns. This agrees with non-Newtonian flow being negligible in larger arteries [7, 9, 11]. However, this statement refers to simple vascular geometries, and is not valid for complex geometries, such as an intracranial aneurysm [10]. The Newtonian assumption underestimated WSS against non-Newtonian models, below their critical shear rates, resulting in larger predicted regions of low and critically low WSS.

4.3 Clinical Relevance

There is a general movement towards patient-specific modeling [38]. This includes the treatment of intracranial aneurysms [5, 10, 25]. Patients are at risk if the areas of low and critically low WSS are significant [10]. Viscosity-limited non-Newtonian schemes may aid in predicting whether an individual is at risk of aneurysm rupture. However, this would require patient-specific blood viscosity because hypertension and diabetes cause elevated viscosity at low shear [39, 40] and the value of the Newtonian viscosity plateau increases with age [14]. In this study, we have shown that subject-specific blood rheology and CFD modeling can be combined to predict aneurysm regions at risk of rupture.
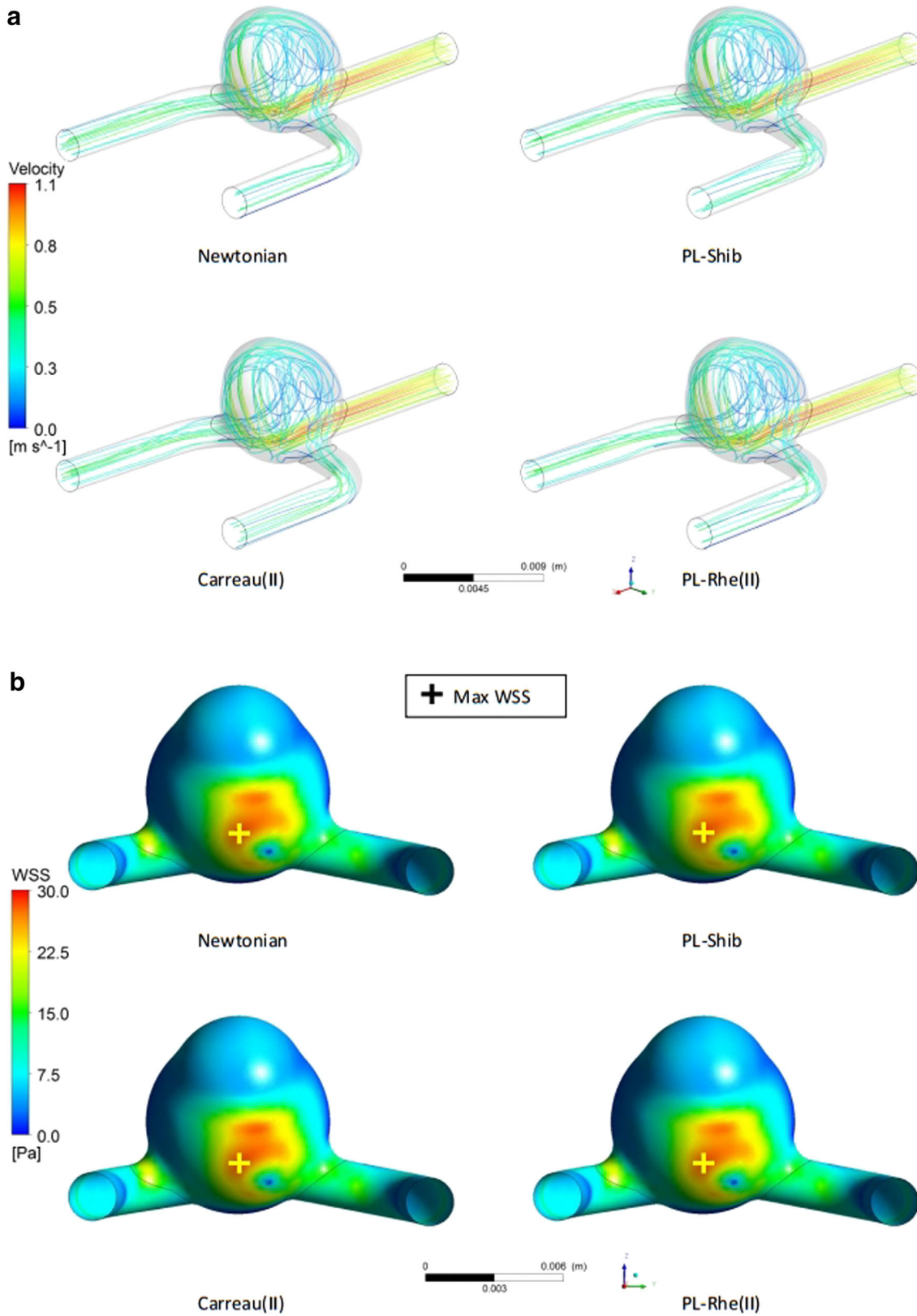
Fig. 5 Viscosity-limited models at peak systole ($t = 0.133$ s). **a** Velocity streamlines and **b** WSS distribution on distal face of aneurysm sac. *Note* PL-Shib refers to *PL-Shibeshi*
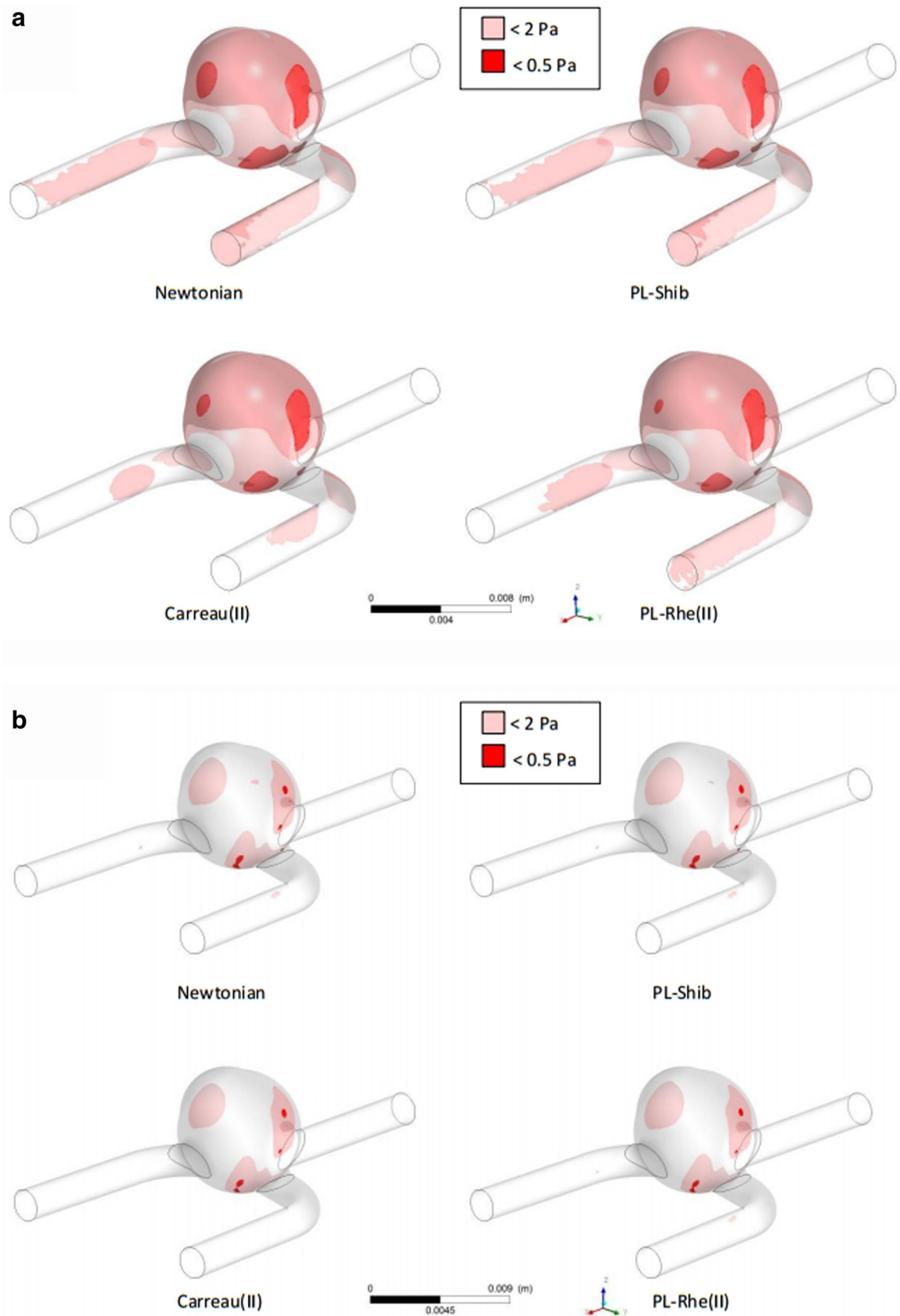
Fig. 6 Low and critically low WSS. **a** Largest difference between Newtonian and non-Newtonian schemes ($t = 0.97$ s). **b** Peak systole ($t = 0.133$ s). *Note* PL-Shib refers to *PL-Shibeshi*

Fig. 7 Area of low and
critically low WSS for
viscosity-limited models.
a Predicted area of low (<2 Pa)
WSS with flow time (note:
Newtonian is obscured by *PL-
Shibeshi*). **b** Predicted area of
critically low (<0.5 Pa) WSS
with flow time. *Note* PL-Shib
refers to *PL-Shibeshi*
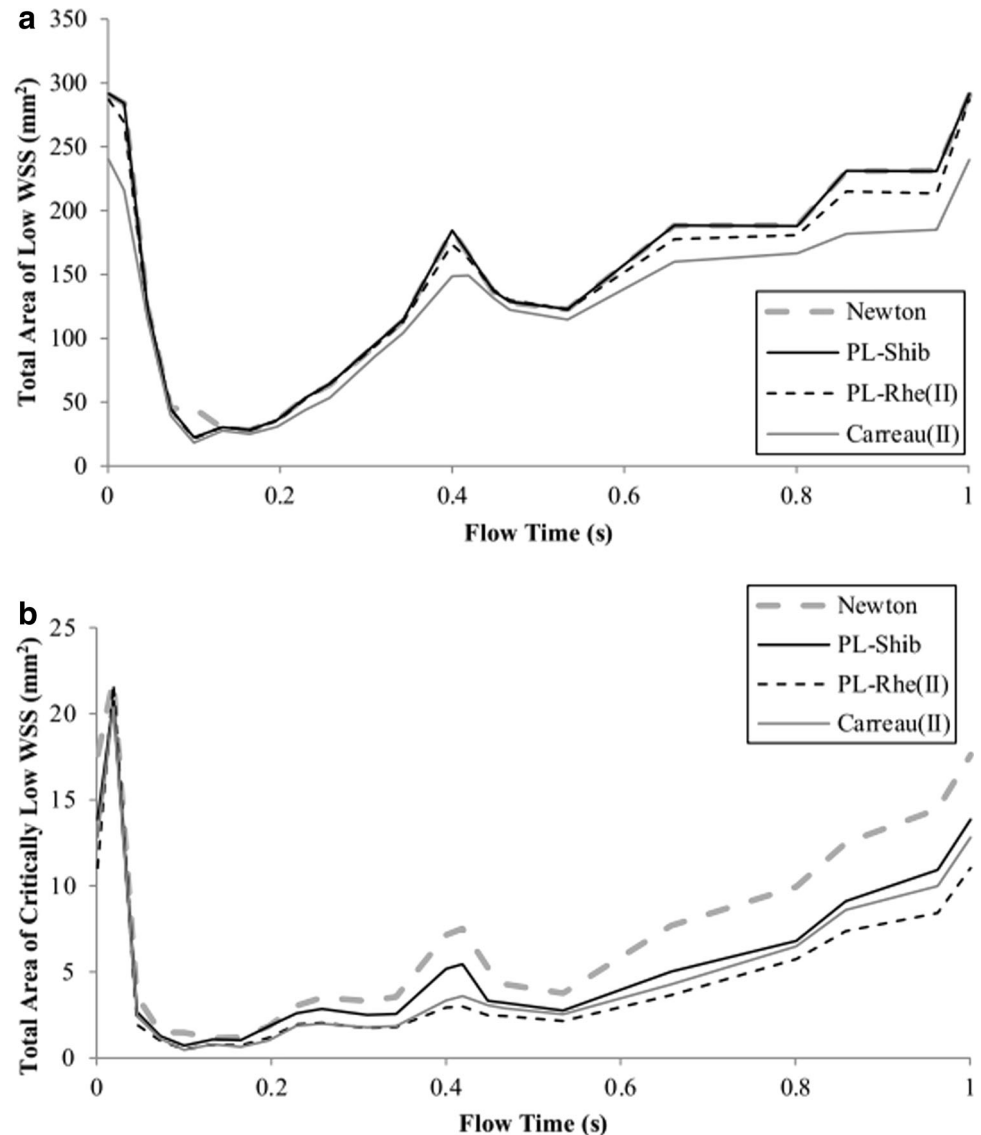
Further development of the model is required before assessment for clinical translation. For example, in our study, the model was assumed to be a rigid body, but in reality the aneurysm wall will flex in response to flow pulses [24]. Lee et al. [41] determined that fluid–structure interaction leads to lower predictions of WSS in a carotid artery compared to CFD. Fluid–structure interaction has been used to model the cardio-vasculature [42, 43] and it is feasible to translate the use of these models into clinical practice. For example, clinical methods used to measure boundary conditions for an individual have been combined with numerical models of heart valves [44]. The model predictions were in good agreement with echo-Doppler-based measurements. The advantage of including a numerical approach is that blood flow patterns and valve stress

can be predicted for the individual [45]. Therefore, there is scope to further develop the model presented in this study into a fluid–structure interaction model [46, 47] and combine it with clinical measurements. Such studies have the potential to better quantify risk of carotid artery aneurysm rupture by considering von Mises stress in the endothelial cells [48]; however, such predictions would require validation.

4.4 Model Reliability

Overall the flow velocities and Reynolds numbers of the Newtonian CFD simulation and experimental results from Van Ooij et al. [2] were similar. The mean velocities observed in the CFD simulations were larger. However, this may also reflect lower resolution for detecting peak

Fig. 8 Effect of shear rate on viscosity-limited model predictions. a Viscosity-shear rate relationship (for approximate range of shear rates observed in simulations). b Shear stress-shear rate relationship (for low shear rates). Note PL-Shib refers to PL-Shibeshi
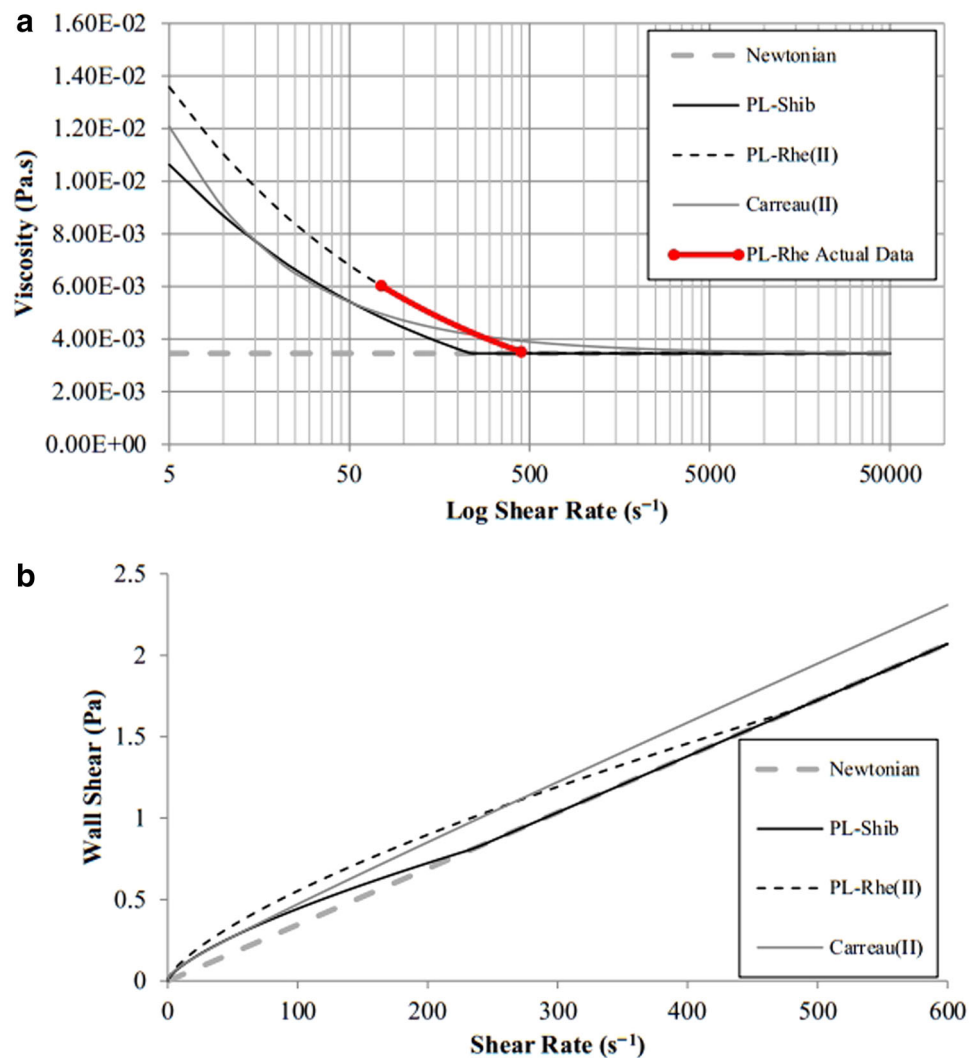
values experimentally with MRI. Moreover, the transient CFD results were similar to those measured from MRI scans and fell within the physiologically relevant range of 100–400 for an intracranial aneurysm [32].

A limitation of this study is that animal (hamster), rather than human, blood was characterized for the non-Newtonian viscosity models *PL-Rhe-I* and *PL-Rhe-II*. However, raw data from a previous study [26] were made available and used to characterize these two viscosity models. The advantage of this was that the full data sets of blood viscosity over a range shear rates were available for fitting to *PL-Rhe-I* and *PL-Rhe-II* models. The raw data included a range of blood viscosity values and their variation with hematocrit level. This enabled the shear-rate-dependent viscosity data best suited to representing human blood to be selected for the study. Most importantly, none of the main conclusions from this study are affected by this limitation.

5 Conclusion

The main findings from this study are that for modeling a saccular intracranial aneurysm at a bifurcation of an anterior communicating artery:

- physiologically accurate parameters of non-Newtonian schemes are required to avoid overestimating viscosity;
- uncapped non-Newtonian descriptions underestimate WSS at high shear rates;
- viscosity-limited parameters prevent excessive thinning at high shear rates and retain non-Newtonian behaviour at low shear rates;
- although predictions from viscosity-limited non-Newtonian models resemble Newtonian models, there are key differences in the predicted total area of critically low WSS.

The assumption that Newtonian blood viscosity models are suitable if vessel diameter is greater than 0.5 mm

cannot always be extrapolated to complex vascular geometries such as saccular intracranial aneurysms. Viscosity-limited non-Newtonian descriptions for blood viscosity are necessary to avoid underestimating WSS and overestimating the size of areas at risk of rupture in intracranial bifurcating artery aneurysms.

References

1. Shojima, M., Oshima, M., Takagi, K., Torii, R., Hayakawa, M., Katada, K., et al. (2004). Magnitude and role of wall shear stress on cerebral aneurysm: Computational fluid dynamic study of 20 middle cerebral artery aneurysms. *Stroke, 35*, 2500–2505.

2. van Ooij, P., Guedon, A., Poelma, C., Schneiders, J., Rutten, M. C. M., Marquering, H. A., et al. (2011). Complex flow patterns in a real-size intracranial aneurysm phantom: Phase contrast MRI compared with particle image velocimetry and computational fluid dynamics. *NMR in Biomedicine, 25*, 14–26.

3. Meng, H., Tutino, V., Xiang, J., & Siddiqui, A. (2014). High WSS or low WSS? Complex interactions of hemodynamics with intracranial aneurysm initiation, growth, and rupture: Toward a unifying hypothesis. *American Journal of Neuroradiology, 35*, 1254–1262.

4. Proust, F., Gerardin, E., & Chazal, J. (2008). Unruptured intracranial aneurysm and microsurgical exclusion: The need of a randomized study of surgery versus natural history. *Journal of Neuroradiology, 35*, 109–115.

5. Valencia, A., Morales, H., Rivera, R., Bravo, E., & Galves, M. (2008). Blood flow dynamics in patient-specific cerebral aneurysm models: The relationship between wall shear stress and aneurysm area index. *Medical Engineering & Physics, 30*, 329–340.

6. Ku, D. (1997). Blood flow in arteries. *Annual Review of Fluid Mechanics, 29*, 399–434.

7. Boyd, J., & Buick, J. (2007). Comparison of Newtonian and non-Newtonian flows in a two-dimensional cartoid artery model using the lattice Boltzmann method. *Physics in Medicine & Biology, 52*, 6215–6228.

8. Gijsen, F., van de Vosse, F., & Janssen, J. (1999). The influence of the non-Newtonian properties of blood on the flow in large arteries: Steady flow in a carotid bifurcation model. *Journal of Biomechanics, 32*, 601–608.

9. Zienkiewicz, O., Tayloe, R., & Nithiarasu, P. (2014). *The finite element method for fluid dynamics*. Oxford: Butterworth-Heinemann.

10. Cavazzuti, M., Atherton, M., Collins, M., & Barozzi, G. (2011). Non-Newtonian and flow pulsatility effects in simulation models of stented intracranial aneurysm. *Proceedings of the Institution of Mechanical Engineers. Part H, Journal of Engineering in Medicine, 225*, 597–609.

11. Kojic, M., Filipovic, N., & Stojanovic, B. (2008). *Computer modeling in bioengineering: Theoretical background, examples and software*. Chichester: Wiley.

12. Lelkes, P., & Gimbrone, M. (2003). *Mechanical forces and the endothelium*. London: Harwood Academic Publishers.

13. Rubenstein, D., Yin, W., & Frame, M. (2012). *Biofluid mechanics*. Oxford: Elsevier.

14. Santos-Galduroz, R., Bueno, O., Yamaga, L., Armani, F., & Galduroz, J. (2012). Influence of blood viscosity to cerebral blood flow in older humans compared to young subjects. *Clinical Neurophysiology, 123*, 117–120.

15. Forsyth, A., Wan, J., Owrutsky, P., Abkarian, M., & Stone, H. (2011). Multiscale approach to link red blood cell dynamics, shear viscosity, and ATP release. *Proceedings of the National Academy of Sciences, 108*, 10986–10991.

16. Wagner, C., Steffen, P., & Svetina, S. (2013). Aggregation of red blood cells: From rouleaux to clot formation. *Comptes Rendues Physique, 14*, 459–469.

17. Chien, S., Usami, S., Dellenback, R., Gregersen, M., Nanninga, L., & Guest, M. (1967). Blood viscosity: Influence of erythrocyte aggregation. *Science, 157*, 829–831.

18. Wang, T., Pan, T., Xing, Z., & Glowinski, R. (2009). Numerical simulation of rheology of red blood cell rouleaux in microchannels. *Physical Reviews E, 79*, 041916.

19. Stuart, J., & Kenny, M. (1980). Blood rheology. *Journal of Clinical Pathology, 33*, 417–429.

20. Wells, R., & Merrill, E. (1962). Influence of flow properties of blood upon viscosity-hematocrit relationships. *Journal of Clinical Investigation, 41*, 1591–1598.

21. Johnston, B., Johnston, P., Corney, S., & Kilpatrick, D. (2004). Non-Newtonian blood flow in human right coronary arteries: Steady state simulations. *Journal of Biomechanics, 37*, 709–720.

22. Ahn, S., Shin, D., Tateshima, S., Tanishita, K., Vinuela, F., & Sinha, S. (2007). Fluid-induced wall shear stress in anthropomorphic brain aneurysm models: MR phase-contrast study at 3 T. *Journal of Magnetic Resonance Imaging, 25*, 1120–1130.

23. Box, F., van der Geest, R., Rutten, M., & Reiber, J. (2005). The influence of flow, vessel diameter, and non-Newtonian blood viscosity on the wall shear stress in a carotid bifurcation model for unsteady flow. *Investigative Radiology, 40*, 277–294.

24. Valen-Sendstad, K., Mardal, K., Mortensen, M., Reif, B., & Langtangen, H. (2011). Direct numerical simulation of transitional flow in patient-specific aneurysm. *Journal of Biomechanics, 44*, 2826–2832.

25. Hassan, T., Timofeev, E., Saito, T., Shimizu, H., Ezura, M., Tominaga, T., et al. (2004). Computational replicas: Anatomic reconstructions of cerebral vessels as volume numerical grids at three-dimensional angiography. *American Journal of Neuroradiology, 25*, 1356–1365.

26. Chatpun, S., & Cabrales, P. (2010). Effects of plasma viscosity modulation on cardiac function during moderate hemodilution. *Asian Journal of Transfusion Science, 4*, 102–108.

27. Chhabra, R., & Richardson, J. (2008). *Non-Newtonian flow and applied rheology: Engineering applications*. Oxford: Butterworth-Heinemann.

28. Wang, C., & Ho, J. (2011). A lattice Boltzmann approach for the non-Newtonian effect in the blood flow. *Computers & Mathematics with Applications, 62*, 75–86.

29. Shibeshi, S. S., & Collins, W. E. (2005). The rheology of blood flow in a branched arterial system. *Applied Rheology, 15*, 398–405.

30. Siebert, M., & Fodor, P. (2009). Newtonian and non-Newtonian blood flows over a backward-facing step—A case study. Boston, *Proceedings of the COMSOL Conference*.

31. Wagshul, M., Eide, P., & Madsen, J. (2011). The pulsating brain: A review of experimental and clinical studies of intracranial pulsatility. *Fluids and Barriers of the CNS, 8*, 5.

32. Mikhal, J., Slump, C. H., & Geurts, B. J. (2012). Simulation of pulsatile flow in cerebral aneurysms: From medical images to

flow and forces. In Y. Murai (Ed.), *aneurysm* (pp. 199–222). Rijeka: InTech.

33. Currie, I. (2002). *Fundamental mechanics of fluids*. New York: CRC Press.

34. Roach, M., Scott, S., & Ferguson, G. (1972). The hemodynamic importance of the geometry of bifurcations in the circle of willis (glass model studies). *Stroke, 3*, 255–267.

35. Hussain, M., Kar, S., & Puniyani, R. (1999). Relationship between power law coefficients and major blood constituents affecting the whole blood viscosity. *Journal of Biosciences, 24*, 329–337.

36. Razavi, A., Shirani, E., & Sadeghi, M. (2011). Numerical simulation of blood pulsatile flow in a stenosed carotid artery using different rheological models. *Journal of Biomechanics, 44*, 2021–2030.

37. Gray, J., Owen, I., & Escudier, M. (2007). Dynamic scaling of unsteady shear-thinning non-Newtonian fluid flows in a large-scale model of a distal anastomosis. *Experiments in Fluids, 43*, 535–546.

38. Öhman, C., Espino, D. M., Heinmann, T., Baleani, M., Delingette, H., & Viceconti, M. (2011). Subject-specific knee joint model: Design of an experiment to validate a multi-body finite element model. *Visual Computer, 27*, 153–159.

39. Letcher, R., Chien, S., Pickering, T., & Laragh, J. (1983). Elevated blood viscosity in patients with borderline essential hypertension. *Hypertension, 5*, 757–762.

40. Skovborg, F., Nielsen, A., Schlichtkrull, J., & Ditzel, J. (1966). Blood viscosity in diabetic patients. *Lancet, 287*, 129–131.

41. Lee, S., Kang, S., Hur, N., & Jeong, S. (2012). A fluid-structure interaction analysis on hemodynamics in carotid artery based on patient-specific clinical data. *Journal of Mechanical Science and Technology, 26*, 3821–3831.

42. Espino, D. M., Shepherd, D. E. T., & Hukins, D. W. L. (2014). Evaluation of a transient, simultaneous, Arbitrary Lagrange Euler based multi-physics method for simulating the mitral heart valve. *Computer Methods in Biomechanics and Biomedical Engineering, 17*, 450–458.

43. Bahraseman, H. G., Hassani, K., Khosravi, A., Navidbakhsh, M., Espino, D. M., Kazemi-Saleh, D., et al. (2013). Estimation of maximum intraventricular pressure: A three-dimensional fluid-structure interaction model. *Biomedical Engineering Online, 12*, 122.

44. Bahraseman, H. G., Hassani, K., Navidbakhsh, M., Espino, D. M., Sani, Z. A., & Fatouraee, N. (2014). Effect of exercise on blood flow through the aortic valve: A combined clinical and numerical study. *Computer Methods in Biomechanics and Biomedical Engineering, 17*, 1821–1834.

45. Bahraseman, H. G., Hassani, K., Khosravi, A., Navidbakhsh, M., Espino, D. M., Fatouraee, N., et al. (2014). Combining numerical and clinical methods to assess aortic valve hemodynamics during exercise. *Perfusion, 29*, 340–350.

46. Li, Z., & Kleinstreuer, C. (2005). Blood flow and structure interactions in a stented abdominal aortic aneurysm model. *Medical Engineering & Physics, 27*, 369–382.

47. Bazilevs, Y., Hsu, M. C., Zhang, Y., Wang, W., Liang, X., Kvamsdal, T., et al. (2010). A fully-coupled fluid-structure interaction simulation of cerebral aneurysms. *Computational Mechanics, 46*, 3–16.

48. Xu, B., Wang, F., Liu, L., Zhang, X., & Ju, H. (2011). Hemodynamics model of fluid–solid interaction in internal carotid artery aneurysms. *Neurosurgical Review, 34*, 39–47.